Published in final edited form as:

Nat Neurosci. 2019 April ; 22(4): 586–597. doi:10.1038/s41593-019-0341-3.

Unique contributions of parvalbumin and cholinergic interneurons in organizing striatal networks during movement

Howard J. Gritton[1,*], **William M. Howe**[1,2,*], **Michael F. Romano**[1,*], **Alexandra G. DiFeliceantonio**[2,3], **Mark A. Kramer**[4], **Venkatesh Saligrama**[5], **Mark E. Bucklin**[1], **Dana Zemel**[1], **Xue Han**[1]

[1]Boston University, Department of Biomedical Engineering, Boston, MA 02215

[2]Icahn School of Medicine at Mt. Sinai, Department of Neuroscience, New York, NY 10129

[3]Yale School of Medicine, Department of Psychiatry, New Haven, CT, 06510

[4]Boston University, Department of Mathematics and Statistics, Boston, MA 02215

[5]Boston University, Department of Electrical and Computer Engineering, Boston, MA 02215

Abstract

Striatal pavalbumin (PV) and cholinergic (CHI) interneurons are poised to play major roles in behavior by coordinating the networks of medium spiny cells that relay motor output. However, the small numbers and scattered distribution of these cells has made it difficult to directly assess their contribution to activity in networks of MSNs during behavior. Here, we build upon recent improvements in single cell calcium imaging combined with optogenetics to test the capacity of PVs and CHIs to affect MSN activity and behavior in mice engaged in voluntarily locomotion. We find that PVs and CHIs have unique effects on MSN activity and dissociable roles in supporting movement. PV cells facilitate movement by refining the activation of MSN networks responsible for movement execution. CHIs, in contrast, synchronize activity within MSN networks to signal the end of a movement bout. These results provide new insights into the striatal network activity that supports movement.

Keywords

striatum; motor; basal ganglia; calcium imaging; GCaMP6f; *in vivo* imaging

Correspondence should be addressed to: Xue Han (xuehan@bu.edu), 44 Cummington Street, Boston, MA 02215. Phone: 617-358-6189.

*These authors contributed equally to this work

Author Contributions

W.M.H. and H.J.G. performed all experiments. M.R. and D.Z. analyzed the data. M.B. contributed software for video processing and data analysis. X.H. supervised the study. W.M.H, H.J.G, M.R., A.G.D, and X.H. wrote the manuscript, and contributed to the interpretation of the results. A.G.D. and MK provided consultation on statistical analysis and on permutation tests. V.S. provided consultation on calcium imaging data analysis and on generalized linear models.

Data Availability Statement

The data that support the findings of this study are available from the corresponding author upon request.

Competing Financial Interests Statement

The authors declare no competing financial interests.

Introduction

Movement disorders including Parkinson's disease and Tourette's syndrome are hypothesized to result from disruptions of basal ganglia circuitry [1–4]. Within the basal ganglia, the dorsal striatum serves as a point of integration between cortical and sub-cortical regions that transforms information provided by these inputs to an output signal that guides behavior [5,6]. Medium spiny projection neurons (MSNs) are the major target of these inputs as well as the primary source of projections from the striatum. These cells comprise roughly 95% of all striatal neurons [7,8], and are traditionally classified based on the target of their output in the Globus Pallidus and the presence of dopamine D1 (direct pathway) or D2 (indirect pathway) receptors [9]. Imbalance between these pathways is thought to contribute to the expression of motor pathologies [2,10,11]. Despite having disparate projection pathways and being differentially regulated by dopamine, recent calcium (Ca^{2+}) imaging studies suggest that these two unique MSNs populations could be uniformly engaged during movement and share a remarkably similar activity profile during normal locomotion [12–15]. These recent findings suggest that coordinated activity in D1 and D2 MSN population supports normal voluntary movement, and disrupting the balance of activity between these two pathways contributes to disease pathology [11]. The mechanisms underlying this coordination are less well understood, although they likely include contributions of local interneurons.

In addition to MSNs, the dorsal striatum also contains multiple populations of interneurons, each of which represent only a small fraction of the total population of cells (<5% per type) [7,16,17]. Though few in number, each interneuron class has the potential to shape striatal activity and function through its innervation of the MSN projection network [18,19]. Two of the best characterized striatal interneurons are the parvalbumin-positive interneurons (PVs) and cholinergic interneurons (CHIs). PVs are GABAergic and can provide a potent source of inhibition on the activity of nearby MSNs to support motor control [20–22]. CHIs are a major source of striatal acetylcholine (ACh) [23,24]. These extensively arborized cells can directly modulate the activity state of MSNs via muscarinic ACh receptors expressed by both D1 and D2 populations of MSNs [25,26], and have likewise been implicated in normal control of motor output [23,27,28].

The unique roles of PVs and CHIs in generating the MSN network dynamics that support movement remain unknown. Efforts to understand how sparsely distributed striatal interneurons interact with MSNs to support behavior have been hampered by a lack of experimental approaches that allow for the simultaneous monitoring of genetically defined interneuron populations in combination with large numbers of MSNs. To gain further insight into interneuron-MSN interactions in support of movement, we utilized a wide-field calcium imaging platform that enabled us to monitor and optogenetically manipulate interneurons, while simultaneously recording calcium dynamics in hundreds of surrounding MSNs in mice during voluntary locomotion. We find that PV and CHI interneuron types differ from one another, and from MSNs, in how they contribute to movement and how they regulate populations of MSN networks that guide behavior. PV interneurons best predict movement and reduce the level of MSN population activity in the dorsal striatum during movement

events. CHIs, in contrast, have a more selective role in recruiting and synchronizing the activity of MSNs during movement to suppress or end a movement bout. Our combined evidence demonstrates the unique capacity of different classes of striatal interneurons to organize networks of MSNs in support of discrete aspects of voluntary locomotion.

Results

Simultaneous monitoring of MSN networks and PVs or CHIs during movement

To simultaneously monitor activity in interneurons in conjunction with the surrounding population of dorsal striatal MSNs, PV-Cre and Chat-Cre mice were injected with AAV-Syn-GCaMP6f [29] to label all striatal neurons with the calcium activity indicator GCaMP6f. AAV-CAG-flex-tdTomato was also co-injected to allow us to label and identify GCaMP6f expressing interneuron cell types (see Figure 1A–C and Figure S1A for experimental timeline). AAV viral mediated flex-targeting allows for highly specific targeting of neuron classes and we found that 96.1±0.2% of tdTomato cells were immunoreactive for PV antibody in PV-Cre mice (Figure S1B–C); and 97.2±0.2% of tdTomato cells were immunoreactive for Chat in Chat-Cre mice (Figure S1D–E) in the area below the imaging window. These numbers were consistent with measures reported previously for these specific transgenic mouse lines [28,30]. Importantly, we also found that <1% of cells co-expressed GCaMP and tdTomato but were immuno-negative for the corresponding Chat or PV antibody in Chat-Cre or PV-Cre mice respectively, demonstrating selectivity.

Calcium responses for the three populations of cells in our experiments were recorded as mice freely ran on a spherical treadmill while tracking movement (Figure 1A). Animals were positioned and imaged underneath a custom microscope equipped with a scientific CMOS camera and imaged at 10X (Figure 1B). This yielded an imaging field of view of 1.343 × 1.343 mm with each pixel corresponding to 1.312 × 1.312 μm^2, allowing in excess of 100 pixels to contribute to a single cell. GCaMP6f excitation was accomplished with a 460 nm LED, and tdTomato excitation with a 567 nm LED (Figure 1B; for a complete description of the labeling, ROI identification, and motion acquisition procedure see Supplemental Methods). As shown in Figure 1C, this approach allowed us to monitor activity in genetically defined interneurons (CHIs: n=5.1±1.1 cells per session, PV: n=4.4±0.8, mean±SEM) in combination with large numbers of surrounding neurons (281.6±34.2, cells per session, mean±SEM). The vast majority of striatal cells are MSNs (~95%); therefore all GCaMP-positive and tdTomato-negative cells were treated as MSNs for the purpose of analysis (see Supplemental Methods for full description of dual labeling approach and analysis). All statistical tests are reported in the corresponding figure legends and are corrected for multiple comparisons. A complete description of all tests and statistical models can be found in Supplemental Methods and the Life Sciences Reporting Summary.

Striatal activity during locomotion

We found that the bulk striatal fluorescence (averaged activity across all cells) increased during periods of movement (high speed) and decreased during periods of no or low movement (low speed, Figure 1D, E, Video S1). For this reason, we focused our analyses around the time of movement onsets as well as peaks in velocity. In a typical 10 min

recording session, 15-20 such locomotion events occurred (Chat-Cre mice, 20.1±4.1 onset events, n=6 mice; PV-Cre mice, 14.9±3.0, n=6 mice; mean±SEM), with the average period of high movement velocity lasting 5.1±0.1 (mean±SEM) seconds. Individual MSN calcium events showed a sharp increase and an exponential decay (see Figure 2A (top; for representative traces). Over all, calcium events were most frequent in MSNs of the three neuron types (Figure 2B), and had the greatest amplitude (Figure S2A). Similar to recent imaging experiments in genetically defined populations of D1 and D2 MSNs, we found that the vast majority of MSNs exhibited a sharp increase in fluorescence at movement onset (Figure 2D), although we did detect a proportion of MSNs that were either negatively (21.4%), or non-modulated (24.2%) by movement (Figure S3). As a population, MSN fluorescence rose coincident with movement onset (Figure 2D–E), peaked coincident with maximum velocity (Figure 2F–G), and then declined as movement slowed (Figure 1D–E).

Calcium events in PV cells were slow to rise and long lasting (Figure 2A (middle), 2C; S2B–C; Video S2), consistent with calcium responses previously noted in PV neurons from cortical regions [31]. Like MSNs, PVs overwhelmingly exhibited increases in fluorescence around motion onset (Figure 2D–E; while only 13.9% of the PV population were negatively modulated at movement onset; see Figure S3C and Figure S4 for a full characterization of positively and the small subset of negatively modulated PVs). The increase in PV activity preceded MSNs by 523.1±304.3ms (mean±SEM; n=13 sessions, Figure 2D; see Figure S5 and Figure S6 for individual examples and supplemental methods for details). Indeed, PV cells also showed the highest proportion of neurons positively modulated in the 500ms before movement onset (Figure S2H), providing further evidence for a rise in PV activity preceding motion onset and MSN activity. Additional analyses showed that in the 1.5 s following a calcium event in the PV population, PVs calcium events were uniquely associated with a positive change in velocity (Figure 2H; S2I).

Calcium events in CHIs had similar event rates across periods of movement as PVs (Figure 2B), and had the smallest area under the curve of all neuron classes (Figure 2A (bottom), 2C), despite having similar rise times and event widths as MSNs (Figure S2B–C). As a population, CHIs showed a modest, but not statistically significant increase in fluorescence at motion onset (Figure 2D–E). Rather, CHI population fluorescence reached maximum intensity approximately 2 seconds after peak velocity (Figure 2F–G, Video S3). Analysis of changes in movement speed following CHI calcium events further indicated that speed dramatically declined following CHI calcium events (Figure 2H; S2I).

Further analyses indicated that CHIs were unique amongst the three cell types in that equal numbers of cells were positively (43.1%) or negatively (37.3%) modulated by motion onset, which likely contributed to the small change in CHI population fluorescence described above (see also Figure S3C). The fluorescence of positively modulated CHIs peaked around maximum velocity (Figure S7C–D) similar to MSNs. In contrast, the negatively modulated CHIs exhibited increased fluorescence 2 seconds after maximum velocity (Figure S7C), the same trend was observed when we considered the CHI population as a whole and described above (Figure 2F–G). Analysis of speed following calcium events in either positively or negatively modulated CHIs revealed that both populations were followed by similar reductions in speed in the 2 seconds after CHI events (Figure S7H). Thus while the two CHI

populations became active at different time points in the movement sequence, each population was active prior to reductions in movement.

Distinct, causal roles for PV and CHI interneurons in movement

In our correlative analysis described above, PV neurons homogeneously become active prior to movement bouts, perhaps providing a unified signal to increase the vigor or specificity of future locomotion. CHIs, while more heterogeneous than PVs or MSNs, as a population become active after peaks in velocity, and calcium events in CHIs were followed by reductions in speed. If each interneuron type is causing rather than tracking these changes in movement speed, manipulation of their activity should impact motor output. To test this hypothesis, we used optogenetics to control activation of PVs and CHIs, while recording locomotion and neuronal activity from MSN and interneuron populations simultaneously. Specifically, the red-shifted, light-activated channelrhodopsin Chrimson [32] was expressed in PV or CHI interneurons using AAV-flex-Chrimson in PV-Cre or Chat-Cre mice. GCaMP6f was expressed in all striatal neurons as above using AAV-Syn-GCaMP6f. Mice were allowed to freely run on the spherical treadmill, while sparse periods (100 frames ~6 seconds) of optogenetic stimulation occurred at random every 25-55 seconds (see Figure 3A and Supplemental Methods).

In PV-Cre mice, if optogenetic stimulation occurred when a mouse was already moving, there was no impact on speed; although stimulation did introduce a transient change in side-to-side directional movement on the spherical treadmill, similar to that seen during endogenous PV events (see supplemental methods, Figure S8A–B; Video S4). Surprisingly, if optogenetic stimulation occurred when animals were at rest, we found that it was sufficient to trigger a transition to movement (Figure 3C). PV-triggered movement bouts plateaued ~1-1.5 seconds after laser onset, consistent with the enhanced period of motor output we witnessed during endogenous PV events (Figure 2H, S2I). Importantly, the same laser stimulation protocol had no impact on the behavior in PV-Cre control mice expressing only tdTomato (without Chrimson), or in Chat-Cre mice expressing Chrimson or tdTomato. Taken together, these results demonstrate that endogenous PV interneuron activity precedes motion onset and that their activation is sufficient to promote movement during periods of inactivity. Furthermore, our predictions regarding unique roles for each interneuron class in modulating behavior, based on the timing of calcium events from each cell class during voluntary movement, were confirmed by optogenetic manipulation of CHIs and PVs.

Consistent with our Ca^{2+} imaging analysis of CHIs, optogenetic stimulation of these cells was sufficient to cause the animal to reduce on-going movement (Figure 3B) without altering direction (Figure S8). This effect was robust, and statistically significant when averaged across all optogenetic stimulation events (Figure 3B). Furthermore, if CHI stimulation occurred when the mouse was at rest, it did not trigger new movement (Figure 3C).The same laser stimulation protocol had no impact on the behavior in Chat-Cre control mice expressing only tdTomato in CHIs. The optogenetic results combined with the Ca^{2+} imaging results from the endogenous activity in the CHIs described above suggest CHIs function to reduce velocity or terminate on-going bouts of locomotion (Figure 3B, Video S5).

Characterization of coordinated MSN and interneuron activity

Similar to other recent reports [12,14], we found that Ca^{2+} dynamics in cells nearby one another (within 100μm) tended to be more correlated than those further away (Figure 4A, see also below 4E). Further, we found that correlations in fluorescence between cells varied by behavioral state (moving or at rest), and increased dramatically during high speed movement periods (Figure 4B), likely due to the increase in Ca^{2+} event rate observed in all neuron types described above (Figure 2B). Finally, this effect of movement state on correlated neural activity was strongest amongst pairs of neurons situated close to one another (Figure 4C, see also Figure S9B), in line with recent findings of spatially organized clusters of dorsal striatal neurons emerging during locomotion [12,14].

In order to get a sense of the correlational structure of Ca^{2+} dynamics between neurons, and control for the potential influence of changes in behavior on these relationships, we calculated asymmetric correlation coefficients [12,33] between pairs of identified MSNs and interneurons. The pairwise correlation between MSN pairs was low (correlation=.08, Figure 4D). When we considered the strength of MSN-MSN correlations by distance, we found, similar to recent studies, that the average correlation between MSNs decreased as the distance between cells increased (Figure 4E), and only those in close proximity to one another were more correlated than chance. We further calculated the proportion of significantly correlated MSN pairs, and found that only a small subset of MSN pairs (~16%; Figure 4F) exhibited such coordination. PVs however showed the highest degree of within-class correlation across the three classes (Figure 4D–E), although only ~25% of PV cells (Figure 4F) were significantly correlated with one another. Unlike MSNs, correlated Ca^{2+} activity between pairs of PV cells was not impacted by distance (Figure 4E). In contrast, CHI pairs were characterized by the weakest within-class correlation and the fewest number of correlated pairs of the three neuron types (Figure 4D–F). The strength of the correlation between CHIs, like PVs, did not vary by the distance between cells (Figure 4E). Thus distance-dependent correlated activity appears to be a feature unique to MSN pairs during voluntary locomotion.

Lastly we considered coordinated activity between MSNs and interneurons (Figure 5A). Across all interneuron-MSN combinations, the proportion of correlated cell pairs decreased with distance, although this decline was sharpest for PV-MSN pairs (Figure 5A, middle), as reflected by the median distance between correlated cells (Figure 5B). In contrast, distance had far less of an influence on correlated CHI-MSN pairs (Figure 5A, right), which were characterized by the largest median distance between related cell pairs (Figure 5B). Combined, these findings are consistent with the prescribed roles of PV cells providing perisomatic inhibition to a local network of nearby MSNs [22], whereas CHI interneurons appear to affect networks of MSNs over greater distances, perhaps via their extensive arborization [23,34].

PVs and CHIs differentially predict movement and MSN activity

Having characterized neural activity surrounding movement, determined a causal role of interneuron activity on movement, and defined the degree of correlated activity between neurons, we next sought to determine how each interneuron population coordinates MSN

activity to control movement. To this end, we first created linear statistical models and tested the capacity of Ca^{2+} dynamics in interneurons to predict changes in the global MSN population fluorescence. Because we found that the population fluorescence in the striatum was highly correlated with both speed and rotation (see Figures S2D, S2G, S9), we considered both factors in our model. We found that the small number of PV cells recorded during a session were equivalent to the power of either speed or rotation in predicting MSN population fluorescence (Figure 6A–B). Since both endogenous and optogenetically evoked PV activity also coincided with changes in movement onset, we further examined whether PV activity could be used as a predictor of speed. We found that the predictive power of the small population of PV neurons (n=4.6) though slightly lower, was similar to that of the entire population of MSNs (n=244.2 neurons/session, Figure 6C–D).

In contrast to PVs, the population of CHIs (n=5.1 neurons/session) were weak predictors of both MSN population activity (Figure 6E–F) and velocity (Figure 6G–H). Importantly, we used regression models as the strength of the prediction for individual neurons would not be affected by whether neurons are positively or negatively modulated by movement. However, given the heterogeneity of CHI responses to motion onset, we conducted additional analyses that considered positive and negatively modulated CHI populations in isolation. We found that the positive and negatively populations did not differ from one another in their predictive relationship toward MSN activity (Figure S7I: left) or speed (Figure S7I: right). Thus, while CHI and PV neurons had similar representations in total number of neurons across recording sessions, only PV neurons were prominent predictors of both instantaneous striatal bulk fluorescence and locomotor output.

PVs and CHIs modulate movement through unique effects on MSN activity

While the predictive modeling described above demonstrates the extent to which interneuron activity can forecast MSN Ca^{2+} dynamics and movement, it does not provide information on whether MSN population dynamics are impacted by changes in PV or CHI activity. Therefore, using the deconvolved calcium fluorescence signal (see Figure S10 and Methods) to align calcium events in each population, we next assessed how the activity within the population of MSNs changed when they coincided with PV or CHI events. Specifically, we compared MSN activity around interneuron events to MSN activity observed by chance around other randomly selected MSN events. We found that on average, MSN population fluorescence was lower than chance when associated with a PV calcium event (Figure 7A), suggesting that PV activity could contribute to a decrease in the MSN population response. In contrast, MSN population fluorescence was elevated when coincident with a CHI calcium event (Figure 7B), suggesting that CHI activity may activate or recruit the MSN population.

Having revealed that interneuron activity coincides with changes in MSN fluorescence, we further considered if this change in fluorescence was a result of changes in coincident activity between MSN pairs. Specifically, we quantified the incidence of MSNs exhibiting coincident calcium events when interneurons are active compared to what would be expected by chance (see Supplemental Methods for details). We found MSN-MSN co-activity was reduced when aligned to PV events, relative to MSNs or CHIs (Figure 7C). Thus the reduction in MSN fluorescence observed during PV activation was concomitant

with a reduction in coincident events in the MSN population. When we performed the same analysis on the optogenetic stimulation sessions, we found that PV activation also reduced the MSN-MSN co-activity during laser on periods when compared to CHI stimulation or endogenous MSN-MSN co-activity (Figure 7D–E). Further MSN population analysis revealed that optogenetic stimulation of PVs did not universally inhibit MSNs, but rather produced heterogeneous changes in MSN activity, including increases in activity in sub-populations of MSNs (Figure S4G). The combined evidence suggests a model whereby PVs support specific movement plans by determining which MSNs are currently active [35].

In contrast, CHI events appeared to have had the opposite effect on the MSN population, and were associated with increased MSN-MSN co-activity; suggesting that CHIs may play a role in enhancing such coincident activity in the population of MSNs (Figure 7C). In line with these observations, optogenetic stimulation of CHIs increased both MSN fluorescence (Figure S11B), the probability of MSN activity (Figure S11F) and MSN-MSN co-activity during laser on periods (Figure 7D–E). To explore whether CHI-mediated enhancement of MSN-MSN co-activity might represent a mechanism underlying the capacity of CHIs to reduce on-going movement, we analyzed motor output during peaks in MSN-MSN co-activity. We found that MSN-MSN co-activity peaks were followed by significant reductions in motor output (Figure 7F), mirroring the reductions in velocity seen in association with endogenous CHI activity (Figure 2H) or optogenetic stimulation of CHIs (Figure 3B).

Together, our data support distinct and dissociable functions of PVs and CHIs in modulating MSNs to support voluntary movement. Optogenetic stimulation of PVs increased future movement, and given their superior capacity to predict MSN population fluorescence and speed, our data strongly supports a specific role for PVs in refining the populations of MSNs recruited during the execution of planned movement. In contrast, CHIs are poor predictors of instantaneous speed or MSN population activity. However, CHI activation is sufficient to reduce movement, an effect that was accompanied by enhanced coordinated activity in the MSN population. Such CHI-mediated MSN coordination represents a unique and previously unknown means by which striatal networks act to terminate on-going movement sequences.

Discussion

To begin to understand how PVs and CHIs modulate striatal MSN activity to support voluntary movement, we developed a large scale two-color imaging assay that enabled us to observe the activity of both interneurons and hundreds of surrounding MSNs in mice as they ran on a spherical treadmill. Because recent studies employing optical imaging to monitor activity in genetically defined D1 versus D2 MSNs did not differentiate these cell types from one another in healthy mice during spontaneous locomotion [11–15] , we considered MSN populations as a single population in our analyses. Distinctions between D1 and D2 MSN activity have been described for goal directed vs habitual behaviors [36,37]. However our data, in the context of other recent imaging studies[11–15], suggest that these distinctions likely reflect striatal network remodeling inherent to learning particular goal directed action sequences. Thus, while our studies specifically sought to characterize the role of two major interneuron populations in modulating general MSN activity and voluntary movement,

future studies could uncover distinct influences of PV and CHI cells on direct or indirect pathway MSNs for different behaviors [30,38].

We found evidence that both PVs and CHIs have activity-behavior relationships that are distinct from MSNs. While MSNs are topographically organized by their relationship to motor output as described previously[12,14], we found that neither PV nor CHI interneuron populations showed a similar anatomical specificity. Further we discovered that PV populations became active prior to MSNs at movement onset, and their calcium activity remains elevated throughout the duration of movement. PVs were also the best predictor of MSN population activity. Interestingly, both endogenous and optogenetically-triggered PV activity produced a reduction in the probability of coincident calcium events occurring in the MSN population. PV interneuron-mediated feedforward inhibition has been hypothesized as a potential mechanism for shutting down active MSNs that are not important for the currently activated motor plan [35].

Although PV cells can provide powerful and reliable feed-forward inhibition to nearby MSNs [19,38], our data suggests their activity largely coincides with periods of movement when MSNs are under the influence of strong excitatory cortical input, subcortical input, and dopamine release. As such, PV signals indeed may serve as an important component for “silencing” non-motor relevant MSNs to create a “de-noised” output condition to facilitate movement execution. This process could aid the selection of individual motor choices through reducing the activity of output neurons that are not integral to on-going behavior, and our data provide support for such a model. Furthermore, given the more narrow anatomical space over which PVs were correlated with MSNs, it is possible that specific subpopulations of PVs could be recruited to inhibit nearby MSNs to bias striatal output. Our finding that PV stimulation could spur new movement, and modulate the trajectory of on-going movement suggests that ill-timed PV activation may be a prominent component of hyperkinetic movement disorders, whereas refined coordination of striatal activity by this population is important for specific movements [21,39]. Taken together, our data support the hypothesis that PV cells play a major role in refining the activation of MSNs to modulate movement execution [21,40]. Future studies will be needed to understand the mechanisms by which this process occurs, but recent evidence suggests that PV neurons can influence MSN networks through direct monosynaptic connections and larger scale di-synaptic circuit interactions [30].

In contrast to MSNs and PVs, increased activity in CHIs was associated with a reduction of ongoing locomotion. We found activity between CHIs was largely uncorrelated during voluntary movement; suggesting that the synchronized activity in CHIs observed in previous studies may be related to a specific response to salient environmental stimuli [41–43]. CHI activity did, however, coincide with recruitment and synchronization of MSNs (Figure 7C), as well as reductions in velocity (Figure 2H). Using optogenetics, we were able to completely recapitulate (Figure 3B, Figure 7D–E) each of these findings illustrating that a major function for CHIs is to coordinate networks of MSNs to trigger the end of a movement bout, and this may represent a key mechanism for cholinergic modulation of motor control. Previous studies in striatal slices have revealed complex actions of acetylcholine in the striatum including both excitatory and inhibitory effects that can alter

MSN activity states [24,44]. The processes by which acetylcholine may organize MSN networks in vivo are less well understood, although the conditions associated with disease states provide insight. Elevated cholinergic tone has been hypothesized to contribute to Parkinson's disease symptoms, in particular akinesia and bradykinesia [28,45], and our results support the idea that augmented cholinergic activity in disease states may promote a pathological synchronization of striatal networks, freezing the dorsal striatum in a state that inhibits movement. The present data offer mechanistic insight into the therapeutic benefits of anti-cholinergic compounds in the treatment of Parkinson's disease [45,46] and other motor disorders associated with elevated cholinergic tone [28]. As recent studies have implicated phasic dopamine release as a mechanism within the striatum to promote movement [47,48], our findings suggest that acetylcholine may act in opposition to this process. More specifically, striatal dopaminergic and cholinergic systems may act synergistically to promote or inhibit movements respectively, and balanced activation within these systems could be critical for the capacity of striatal networks to support dynamic behaviors.

The results reported here specifically relate to striatal control of volitional movement, deficits in which are prominent features of several disorders. Interestingly, evidence suggests that goal-directed actions are often preserved in patients with neurodegenerative disorders like Parkinson's disease [2,49,50]. Thus identifying how MSN and interneuron populations interact to control self-generated locomotion is a crucial step in the effort to develop new treatments for a major, debilitating symptom of these disorders. Our data provide a foundation, and more broadly highlight that as potential therapies for movement disorders are explored, striatal function should not be considered as a monolithic whole, but rather a mosaic of projection cell networks differentially regulated by neuromodulators and local interneurons to support diverse functions.

Supplementary Material

Refer to Web version on PubMed Central for supplementary material.

Acknowledgements

We thank members of the Han Lab for suggestions on the manuscript. We would also like to thank Jun Li and Erik Kolaczyk for their useful insights on data analysis and statistical analysis. We would also like to acknowledge Christopher Harvey and Daniel Dombeck for their help on the construction of the 3D spherical tracking system. This work was supported by the NIH Director's Office (1DP2NS082126 to X.H.), NINDS (1R01NS081716 to X.H., 1R01NS087950 to X.H.), the Grainger Foundation to X.H., and the Pew Foundation to X.H.

References

1. Albin RL et al. Increased ventral striatal monoaminergic innervation in Tourette syndrome. Neurology 61, 310–315 (2003). [PubMed: 12913189]
2. Albin RL, Young AB & Penney JB The functional anatomy of basal ganglia disorders. Trends Neurosci 12, 366–375, doi:0166-2236(89)90074-X [pii] (1989). [PubMed: 2479133]
3. Obeso JA et al. Pathophysiology of the basal ganglia in Parkinson's disease. Trends Neurosci 23, S8–19 (2000). [PubMed: 11052215]
4. Penney JB Jr. & Young AB Striatal inhomogeneities and basal ganglia function. Mov Disord 1, 3–15, doi:10.1002/mds.870010102 (1986). [PubMed: 2848190]

5. Mailly P, Aliane V, Groenewegen HJ, Haber SN & Deniau JM The rat prefrontostriatal system analyzed in 3D: evidence for multiple interacting functional units. J Neurosci 33, 5718–5727, doi: 10.1523/JNEUROSCI.5248-12.201333/13/5718 [pii] (2013). [PubMed: 23536085]
6. Voorn P, Vanderschuren LJ, Groenewegen HJ, Robbins TW & Pennartz CM Putting a spin on the dorsal-ventral divide of the striatum. Trends Neurosci 27, 468–474, doi:10.1016/j.tins.2004.06.006 S0166-2236(04)00190-0 [pii] (2004). [PubMed: 15271494]
7. Graveland GA & DiFiglia M The frequency and distribution of medium-sized neurons with indented nuclei in the primate and rodent neostriatum. Brain Res 327, 307–311, doi:0006-8993(85)91524-0 [pii] (1985). [PubMed: 3986508]
8. Tepper JM, Wilson CJ & Koos T Feedforward and feedback inhibition in neostriatal GABAergic spiny neurons. Brain Res Rev 58, 272–281, doi:S0165-0173(07)00227-5 [pii] 10.1016/j.brainresrev.2007.10.008 (2008). [PubMed: 18054796]
9. Gerfen CR et al. D1 and D2 dopamine receptor-regulated gene expression of striatonigral and striatopallidal neurons. Science 250, 1429–1432 (1990). [PubMed: 2147780]
10. DeLong MR Primate models of movement disorders of basal ganglia origin. Trends Neurosci 13, 281–285 (1990). [PubMed: 1695404]
11. Parker JG et al. Diametric neural ensemble dynamics in parkinsonian and dyskinetic states. Nature 557, 177–182, doi:10.1038/s41586-018-0090-610.1038/s41586-018-0090-6 [pii] (2018). [PubMed: 29720658]
12. Barbera G et al. Spatially Compact Neural Clusters in the Dorsal Striatum Encode Locomotion Relevant Information. Neuron 92, 202–213, doi:S0896-6273(16)30530-X [pii] 10.1016/j.neuron.2016.08.037 (2016). [PubMed: 27667003]
13. Cui G et al. Concurrent activation of striatal direct and indirect pathways during action initiation. Nature 494, 238–242, doi:10.1038/nature11846 nature11846 [pii] (2013). [PubMed: 23354054]
14. Klaus A et al. The Spatiotemporal Organization of the Striatum Encodes Action Space. Neuron 96, 949, doi:S0896-6273(17)31024-3 [pii] 10.1016/j.neuron.2017.10.031 (2017).
15. Meng C et al. Spectrally Resolved Fiber Photometry for Multi-component Analysis of Brain Circuits. Neuron 98, 707–717 e704, doi:S0896-6273(18)30296-4 [pii] 10.1016/j.neuron.2018.04.012 (2018). [PubMed: 29731250]
16. Oorschot DE Cell Types in the Different Nuclei of the Basal Ganglia. Hbk Behav Neurosci 20, 63–74 (2010).
17. Roberts RC, Gaither LA, Peretti FJ, Lapidus B & Chute DJ Synaptic organization of the human striatum: a postmortem ultrastructural study. J Comp Neurol 374, 523–534, doi:10.1002/(SICI)1096-9861(19961028)374:4<523::AID-CNE4>3.0.CO;2-3 [pii] 10.1002/(SICI)1096-9861(19961028)374:4<523::AID-CNE4>3.0.CO;2-3 (1996). [PubMed: 8910733]
18. Tepper JM & Bolam JP Functional diversity and specificity of neostriatal interneurons. Curr Opin Neurobiol 14, 685–692, doi:S0959-4388(04)00155-2 [pii] 10.1016/j.conb.2004.10.003 (2004). [PubMed: 15582369]
19. Tepper JM, Tecuapetla F, Koos T & Ibanez-Sandoval O Heterogeneity and diversity of striatal GABAergic interneurons. Front Neuroanat 4, 150, doi:10.3389/fnana.2010.00150 (2010). [PubMed: 21228905]
20. Gittis AH et al. Selective inhibition of striatal fast-spiking interneurons causes dyskinesias. J Neurosci 31, 15727–15731, doi:10.1523/JNEUROSCI.3875-11.201131/44/15727 [pii] (2011). [PubMed: 22049415]
21. Gittis AH, Nelson AB, Thwin MT, Palop JJ & Kreitzer AC Distinct roles of GABAergic interneurons in the regulation of striatal output pathways. J Neurosci 30, 2223–2234, doi:10.1523/JNEUROSCI.4870-09.201030/6/2223 [pii] (2010). [PubMed: 20147549]
22. Koos T & Tepper JM Inhibitory control of neostriatal projection neurons by GABAergic interneurons. Nat Neurosci 2, 467–472, doi:10.1038/8138 (1999). [PubMed: 10321252]
23. Bolam JP, Wainer BH & Smith AD Characterization of cholinergic neurons in the rat neostriatum. A combination of choline acetyltransferase immunocytochemistry, Golgi-impregnation and electron microscopy. Neuroscience 12, 711–718, doi:0306-4522(84)90165-9 [pii] (1984). [PubMed: 6382048]

24. Calabresi P, Centonze D, Gubellini P, Pisani A & Bernardi G Acetylcholine-mediated modulation of striatal function. Trends Neurosci 23, 120–126, doi:S0166-2236(99)01501-5 [pii] (2000). [PubMed: 10675916]
25. Surmeier DJ, Ding J, Day M, Wang Z & Shen W D1 and D2 dopamine-receptor modulation of striatal glutamatergic signaling in striatal medium spiny neurons. Trends Neurosci 30, 228–235, doi:S0166-2236(07)00069-0 [pii] 10.1016/j.tins.2007.03.008 (2007). [PubMed: 17408758]
26. Yan Z, Flores-Hernandez J & Surmeier DJ Coordinated expression of muscarinic receptor messenger RNAs in striatal medium spiny neurons. Neuroscience 103, 1017–1024, doi:S0306452201000392 [pii] (2001). [PubMed: 11301208]
27. Cachope R et al. Selective activation of cholinergic interneurons enhances accumbal phasic dopamine release: setting the tone for reward processing. Cell Rep 2, 33–41, doi:10.1016/j.celrep.2012.05.011 S2211-1247(12)00136-2 [pii] (2012). [PubMed: 22840394]
28. Kondabolu K et al. Striatal cholinergic interneurons generate beta and gamma oscillations in the corticostriatal circuit and produce motor deficits. Proc Natl Acad Sci U S A 113, E3159–3168, doi:10.1073/pnas.1605658113 1605658113 [pii] (2016). [PubMed: 27185924]
29. Chen TW et al. Ultrasensitive fluorescent proteins for imaging neuronal activity. Nature 499, 295–300, doi:10.1038/nature12354 nature12354 [pii] (2013). [PubMed: 23868258]
30. Lee K et al. Parvalbumin Interneurons Modulate Striatal Output and Enhance Performance during Associative Learning. Neuron 93, 1451–1463 e1454, doi:S0896-6273(17)30141-1 [pii] 10.1016/j.neuron.2017.02.033 (2017). [PubMed: 28334608]
31. Pinto L & Dan Y Cell-Type-Specific Activity in Prefrontal Cortex during Goal-Directed Behavior. Neuron 87, 437–450, doi:10.1016/j.neuron.2015.06.021 S0896-6273(15)00564-4 [pii] (2015). [PubMed: 26143660]
32. Klapoetke NC et al. Independent optical excitation of distinct neural populations. Nat Methods 11, 338–346, doi:10.1038/nmeth.2836 nmeth.2836 [pii] (2014). [PubMed: 24509633]
33. Schwartz TH et al. Networks of coactive neurons in developing layer 1. Neuron 20, 541–552, doi:S0896-6273(00)80993-9 [pii] (1998). [PubMed: 9539127]
34. Wilson CJ, Chang HT & Kitai ST Firing patterns and synaptic potentials of identified giant aspiny interneurons in the rat neostriatum. J Neurosci 10, 508–519 (1990). [PubMed: 2303856]
35. Moyer JT, Halterman BL, Finkel LH & Wolf JA Lateral and feedforward inhibition suppress asynchronous activity in a large, biophysically-detailed computational model of the striatal network. Front Comput Neurosci 8, 152, doi:10.3389/fncom.2014.00152 (2014). [PubMed: 25505406]
36. Smith KS & Graybiel AM Habit formation coincides with shifts in reinforcement representations in the sensorimotor striatum. J Neurophysiol 115, 1487–1498, doi:10.1152/jn.00925.2015 jn.00925.2015 [pii] (2016). [PubMed: 26740533]
37. Thorn CA, Atallah H, Howe M & Graybiel AM Differential dynamics of activity changes in dorsolateral and dorsomedial striatal loops during learning. Neuron 66, 781–795, doi:10.1016/j.neuron.2010.04.036 S0896-6273(10)00329-6 [pii] (2010). [PubMed: 20547134]
38. Owen SF, Berke JD & Kreitzer AC Fast-Spiking Interneurons Supply Feedforward Control of Bursting, Calcium, and Plasticity for Efficient Learning. Cell 172, 683–695 e615, doi:S0092-8674(18)30040-0 [pii] 10.1016/j.cell.2018.01.005 (2018). [PubMed: 29425490]
39. Kalanithi PS et al. Altered parvalbumin-positive neuron distribution in basal ganglia of individuals with Tourette syndrome. Proc Natl Acad Sci U S A 102, 13307–13312, doi:0502624102 [pii] 10.1073/pnas.0502624102 (2005). [PubMed: 16131542]
40. Planert H, Szydlowski SN, Hjorth JJ, Grillner S & Silberberg G Dynamics of synaptic transmission between fast-spiking interneurons and striatal projection neurons of the direct and indirect pathways. J Neurosci 30, 3499–3507, doi:10.1523/JNEUROSCI.5139-09.201030/9/3499 [pii] (2010). [PubMed: 20203210]
41. Adler A, Katabi S, Finkes I, Prut Y & Bergman H Different correlation patterns of cholinergic and GABAergic interneurons with striatal projection neurons. Front Syst Neurosci 7, 47, doi:10.3389/fnsys.2013.00047 (2013). [PubMed: 24027501]

42. Apicella P Tonically active neurons in the primate striatum and their role in the processing of information about motivationally relevant events. Eur J Neurosci 16, 2017–2026, doi:2262 [pii] (2002). [PubMed: 12473069]
43. Kimura M, Rajkowski J & Evarts E Tonically discharging putamen neurons exhibit set-dependent responses. Proc Natl Acad Sci U S A 81, 4998–5001 (1984). [PubMed: 6589643]
44. Shen W, Hamilton SE, Nathanson NM & Surmeier DJ Cholinergic suppression of KCNQ channel currents enhances excitability of striatal medium spiny neurons. J Neurosci 25, 7449–7458, doi: 25/32/7449 [pii] 10.1523/JNEUROSCI.1381-05.2005 (2005). [PubMed: 16093396]
45. Lang AE & Lees AJ Anticholinergic therapies in the treatment of Parkinson's disease. Mov Disord 17 Suppl 4, S7–12, doi:10.1002/mds.5556 (2002). [PubMed: 12211135]
46. Pisani A et al. Targeting striatal cholinergic interneurons in Parkinson's disease: focus on metabotropic glutamate receptors. Neuropharmacology 45, 45–56, doi:S0028390803001370 [pii] (2003). [PubMed: 12814658]
47. da Silva JA, Tecuapetla F, Paixao V & Costa RM Dopamine neuron activity before action initiation gates and invigorates future movements. Nature 554, 244–248, doi:10.1038/nature25457 nature25457 [pii] (2018). [PubMed: 29420469]
48. Howe MW & Dombeck DA Rapid signalling in distinct dopaminergic axons during locomotion and reward. Nature 535, 505–510, doi:nature18942 [pii] 10.1038/nature18942 (2016). [PubMed: 27398617]
49. Bichsel O et al. Functionally separated networks for self-paced and externally-cued motor execution in Parkinson's disease: Evidence from deep brain recordings in humans. Neuroimage, doi:S1053-8119(18)30410-5 [pii] 10.1016/j.neuroimage.2018.05.012 (2018).
50. Redgrave P et al. Goal-directed and habitual control in the basal ganglia: implications for Parkinson's disease. Nature reviews. Neuroscience 11, 760–772, doi:10.1038/nrn2915 nrn2915 [pii] (2010). [PubMed: 20944662]

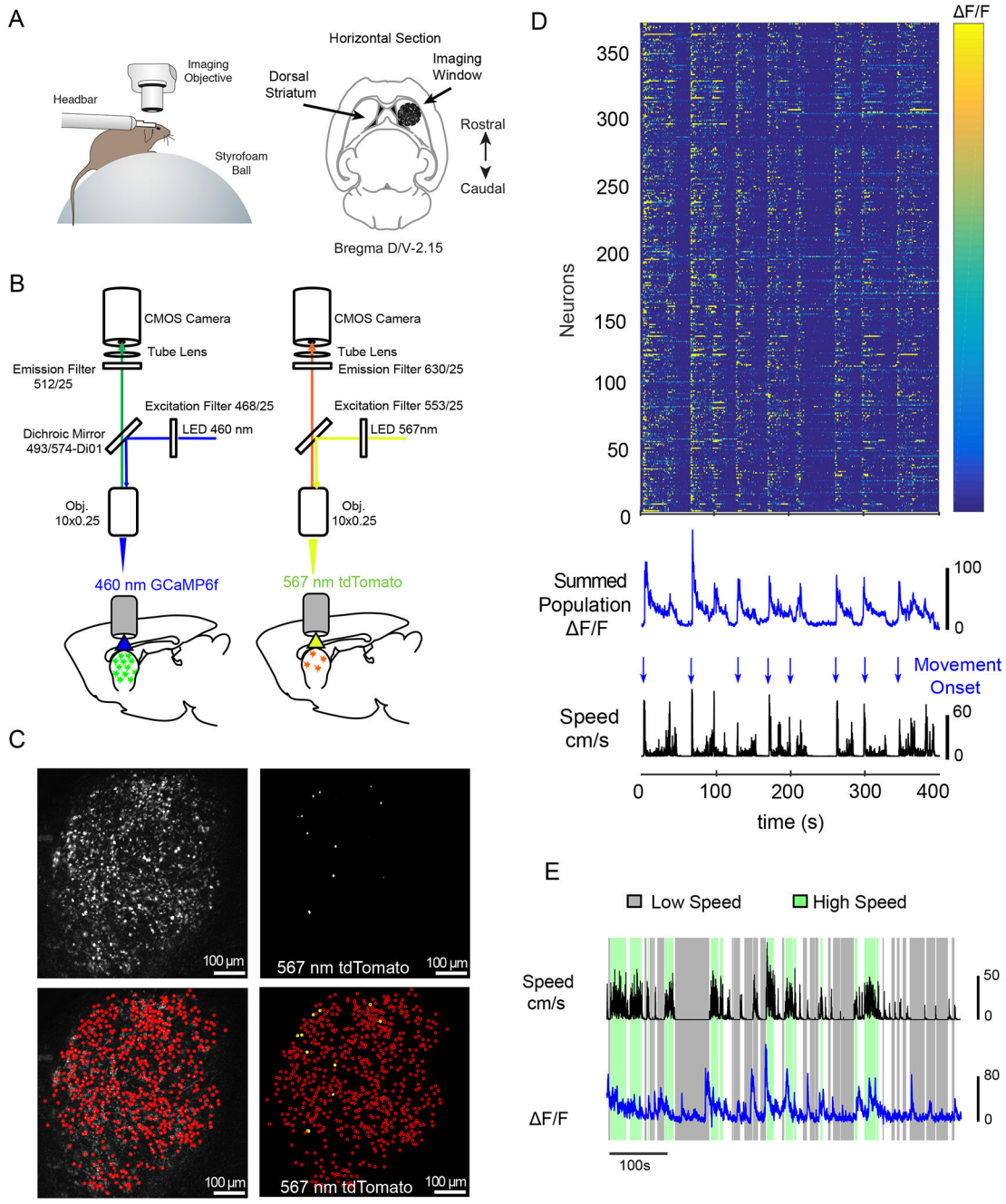

Figure 1: Experimental Paradigm and Imaging Protocol.

(A) Left, Schematic of behavioral paradigm showing a head-fixed mouse under the imaging scope positioned on a spherical treadmill. The animal's position and movement were simultaneously acquired along with Ca^{2+} imaging data. **Right**, Anatomical schematic showing placement of the imaging window for striatal recordings. **(B)** Imaging protocol. Recording sessions began with calcium imaging of GCaMP6f in the dorsal striatum using a 460nm illumination LED (left), followed by tdTomato imaging with a 567nm illumination LED (right). **(C)** Wide-field images from each recording condition described in (B) from a

PV-Cre mouse. **Left, top**, Max-minus-minimum pixel intensity map of GCAMP6f fluorescence across all frames. **Bottom**, same GCaMP6f image overlaid with manually identified individual GCaMP6f expressing cells (red circles). **Right, top**, tdTomato fluorescence, max pixel intensity map across all frames. Bottom, same tdTomato image overlaid with identified GCaMP6f expressing cells (yellow circles indicate cells co-expressing GCaMP6f and tdTomato). Recording sessions yielded a large number of total neurons (n=281.6±34.2, mean±SEM, across 28 recording sessions) with a substantially smaller number of interneuron cell types (CHIs: n=5.1±1.1 cells per session, 10 sessions in 6 animals; PV: n=4.4±0.8, mean±SEM across 18 sessions in 6 animals). **(D)** Color map showing GCaMP6f activity from 375 neurons (371 MSNs and 4 PVs) recorded during a representative 10 minute long imaging session from a PV-Cre animal. Below, summed population GCaMP6f fluorescence (blue:top) and linear velocity (speed:black) shown in the color map. Arrows indicate movement onsets (blue). Movement onsets and offsets were determined based on thresholded changes in movement speed independently (see supplementary methods). **(E)** Extracted movement speed (black) and summed population GCaMP6f fluorescence of all neurons (blue curve, summed from 544 MSNs and 3 CHI) from a representative Chat-Cre animal. Highlighting indicates periods of sustained high movement speed (green: > 5cm/s sustained) or low movement speed (gray: <1 cm/s, sustained: see supplementary methods for details).

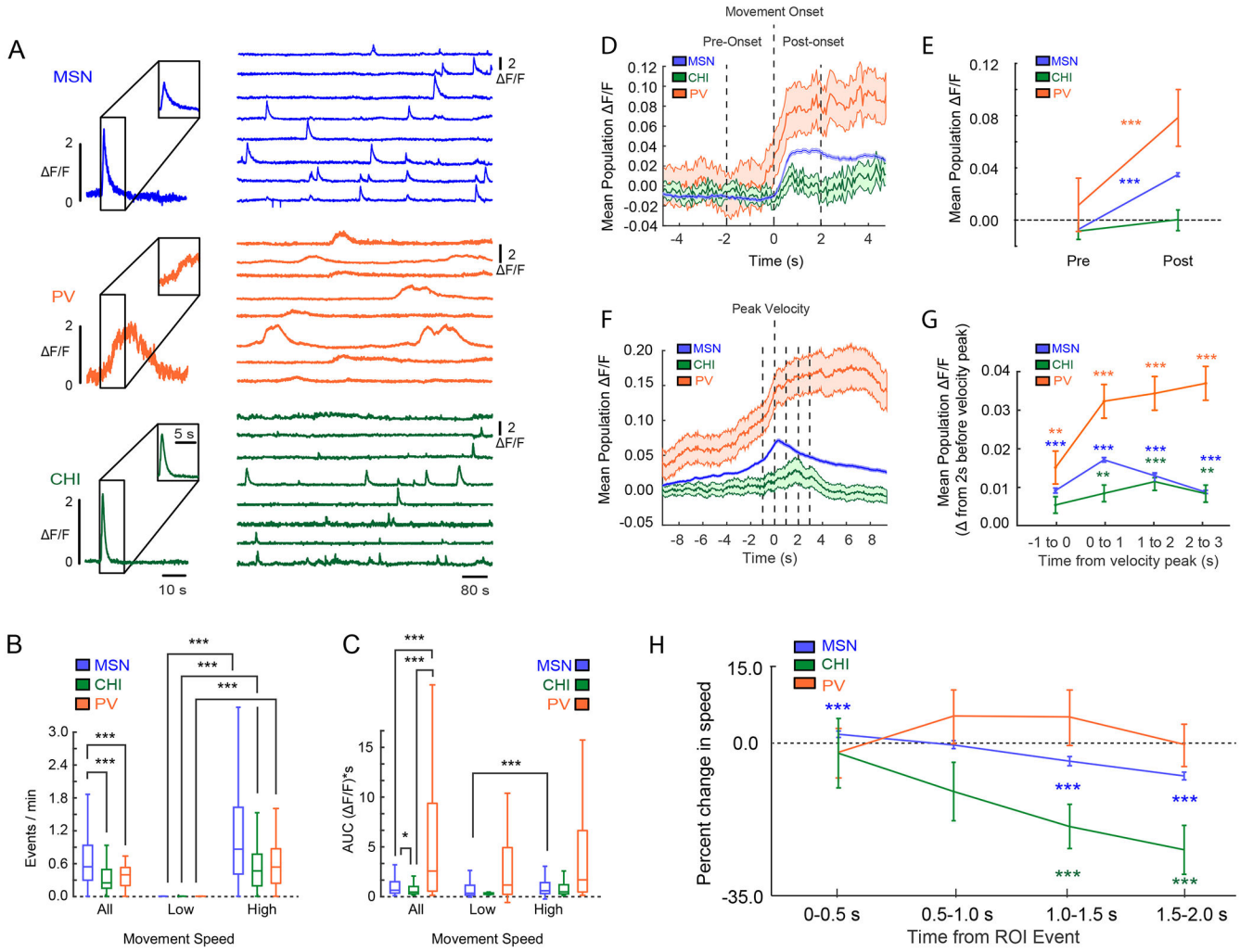

Figure 2: Striatal Population Activity Correlates with Discrete Aspects of Movement.

(A) Representative calcium events from the three types of neurons recorded; MSNs (top), PV cells (middle) and CHIs (bottom). **(B)** Calcium event rates during high versus low speed periods. Event rates for all neurons increased during periods of high movement speed (Sign-test, MSN: sign=6999, n=7518, 237 ties, p=0; CHI: sign=43, n=47 neurons, 4 ties, p=2.78e-09; PV: sign=66, n=72 neurons, 7 ties, p=7.26e-14, across 28 sessions in 12 animals). **(C)** Calcium event shape assessed as area under the curve (AUC), with PVs' having the largest, and CHIs the smallest waveforms (Kruskal-Wallis, X^2 (2)=37.3, p=8.02e-09, n_{MSN}=7727, n_{PV}=78, n_{CHI}=50; mean ranks: MSN: 3.92e+03, PV: 5.36e+03, CHI: 3.13e+03; Tukey's HSD post-hoc, PV vs MSN: p=7.58e-08, PV vs CHI, p=1.80e-07, MSN vs CHI: 0.038). This distinction was conserved during both high and low speed periods. MSNs also showed a small but significant increase in AUC between low and high speed movement periods, while PVs and CHIs were unchanged (Sign-test, MSN: sign=1190, n=1813 neurons, 0 ties, p=2.55e-40; CHI: sign=8, n=11 neurons, 0 ties, p=0.23; PV: sign=5, n=13 neurons, 0 ties, p=0.58). *=p<0.05, ***=p<0.001. **(D)** Mean population fluorescence of each cell class relative to movement onset. Line and shaded regions indicate the mean ±

SEM. **(E)** Quantification of the change in fluorescence between the pre-onset and post-onset windows around movement onset. All cell classes showed an increase in mean fluorescence from pre-onset, except CHIs (change from pre-onset; Sign-test, MSNs: sign=2540, n=7755 neurons from 12 mice, p=1.60e-202; CHIs: sign=25, n=51 neurons from 6 mice, p=1; PVs: sign=16, n=79 neurons from 6 mice, p=9.44e-08). In PVs, the increase in fluorescence around motion onset began 523.1±304.3ms before MSNs. Line plots and error bars indicate the mean ± SEM. **(F)** Mean population fluorescence of each cell class relative to peak velocity. Line and shaded regions indicate the mean ± SEM. **(G)** Quantification of fluorescence across the peak velocity time period. MSNs and PV cells when compared to baseline (2 seconds before peak velocity) showed significantly elevated fluorescence in the 1 second prior to peak velocity and in each 1 second time bin following. CHIs did not show significantly higher fluorescence until after peak velocity plateauing in the 1-2 second post-peak bin. Line plots and error bars indicate mean ± SEM. (Mixed-effects model; ANOVA for interaction of cell type and time bin: $F(10,6.11e+06) = 9.52$, p=4.91e-16; fluorescence for PVs at bin 1 (−1 to 0 seconds pre-peak): $t(48198)=3.08$, p =0.00278 vs baseline; fluorescence for MSNs −1 to 0 seconds following event, $t(6.00e+06)=21.6$, p=3.34e-103 vs baseline, fluorescence for CHIs 0-1 seconds following event, $t(59244)=2.93$, p=0.00428 vs baseline). **(H)** Normalized change in movement speed centered on calcium events sorted by cell class. Line plots and error bars indicate mean ± SEM. Analysis revealed a significant interaction between time bin and cell type (Mixed-effects model, ANOVA $F(8,39260)=3.61$, p=0.00034), so comparisons were broken down by cell type. CHI calcium events were followed by a significant decrease in speed compared with events from the other two cell types. Comparisons of time windows to baseline, 0-500ms (CHIs: $t(245)=-0.33$, p=0.81; PVs: $t(385)=-0.42$, p=0.81; MSNs: $t(38630)=5.0$, p=1.9e-06); 500-1000ms (CHIs: $t(245)=-2.0$, p=0.089; PVs: $t(385)=1.02$, p=0.52; MSNs: $t(38630)=-0.76$, p=0.59), 1000-1500ms (CHIs: $t(245)=-3.6$, p=9.2e-04; PVs: $t(385)=0.95$, p=0.52; MSNs: $t(38630)=-10.0$, p=9.1e-23), 1500-2000ms (CHIs: $t(245)=-4.68$, $p<0.001$; PVs: $t(385)=-0.19$, p=0.85; MSNs: $t(38630)=-18.4$, p=3.83e-74) Benjamini-Hochberg corrected across all cell types and time bins (n=12 comparisons; $n_{MSN}=7727$, $n_{CHI}=50$, and $n_{PV}=78$. A total of 30 cells out of 7855 did not produce an event that was included in this analysis, see methods for details; MSN, n=28 cells; PV, n=1 cell; CHI, n=1 cell). For all box plot figures, middle lines indicate the median, lower and upper edges of the box indicate quartiles below and above the median, and upper and lower whiskers indicate the points furthest from the median whose value did not exceed 1.5 times the first-to-third quartile range above the third quartile or below the first quartile. All sign-tests were two-sided.

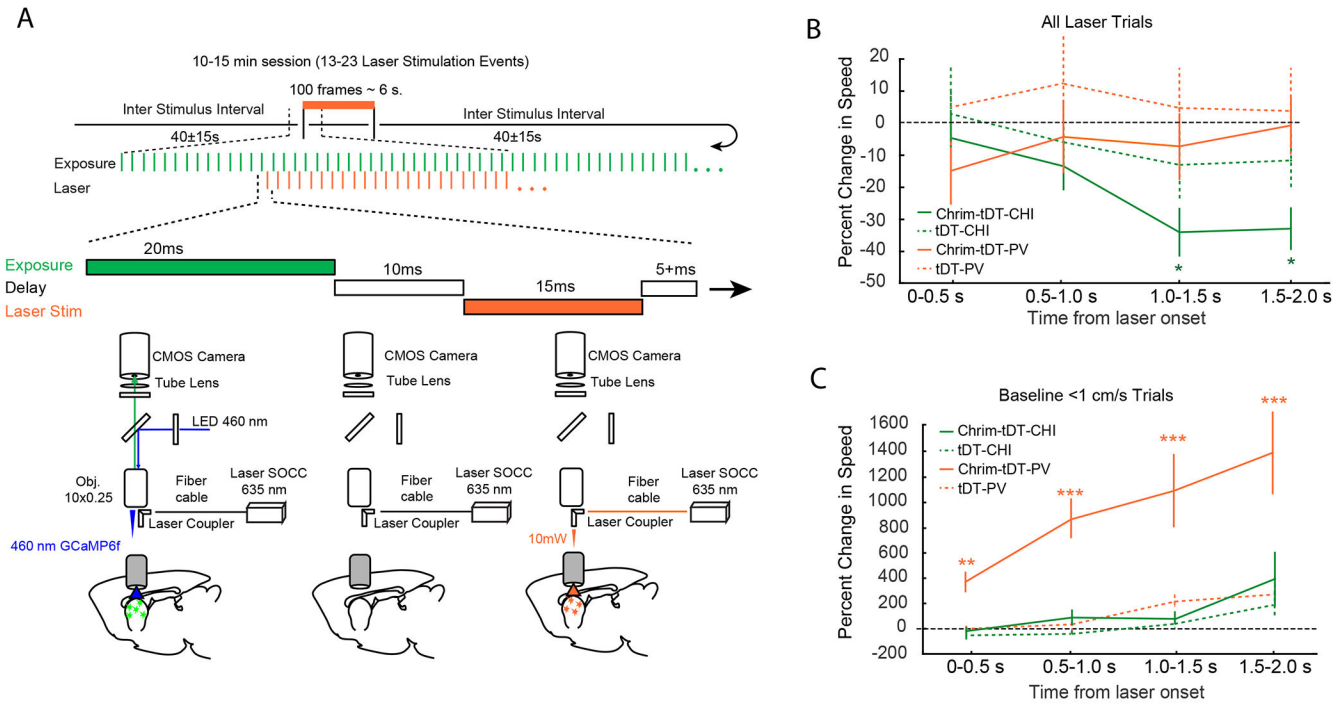

Figure 3: Optogenetic Stimulation of Interneuron Populations Modulates Movement.

(A) Simultaneous optogenetic stimulation and imaging experimental design. (top) Animals were imaged over 10-15 continuous minutes and received 13-23 trials of optogenetic stimulation with an ITI of 40±15seconds. Each trial consisted of 100 laser stimulation pulses at ~15 Hz. Red laser light was pulsed between GCaMP6f imaging frames. (bottom), Cartoon depicting alternating GCaMP6f image acquisition and red laser light delivery for Chrimson activation through the imaging window across successive frames. **(B)** Normalized change in movement speed at laser onset for PV-Chrimson and Chat-Chrimson mice for all trials (n=4 PV-Chrimson mice, and n=4 Chat-Chrimson mice, 2 sessions for each mouse). Line plots and error bars indicate mean ±SEM. Significant reductions in speed coincided with laser onset only in Chat-Chrimson mice (Mixed-effects model, ANOVA: $F(4,645)=6.7$, $p < 0.001$; comparisons of time windows: 0-500ms; $t(645)= -0.91$, $p=0.36$, 500-1000ms; $t(645)=-1.8$, $p=0.11$, 1000-1500ms; $t(645)=-3.8$, $p=6.2e-04$; 1500-2000ms, $t(645)=-3.6$, $p=8.1e-04$. *=p<0.01, Benjamini-Hochberg corrected). This effect was not present in PV-Chrimson mice (Mixed-effects model, ANOVA: $F(4,575)=1.4$, $p=0.24$), or in control mice (n=4 PV-tDTomato mice, and n=4 Chat-tDTomato mice, 2 sessions for each mouse; PV-tDTomato mice: Mixed-effects model, ANOVA: $F(4,580)=6.0$, $p=0.60$; Chat-tDTomato mice: Mixed-effects model, ANOVA: $F(4,580)=2.2$, $p=0.07$). **(C)** Normalized change in movement speed following laser onset for PV-Chrimson and Chat-Chrimson mice when stimulation occurred during periods of low movement. Line plots and error bars indicate mean ± SEM. Laser stimulation increased movement only in PV-Chrimson mice (Mixed-Effects Model, ANOVA $F(4,200)=5.4$, $p=4.0e-04$; baseline vs time=0-500ms: $t(200)=3.16$, $p =0.0018$; baseline vs time=500-1000ms: $t(200)=4.3$, $p=6.2e-05$; baseline vs time=1000-1500: $t(200)=3.6$, $p=6.0e-04$; baseline vs time=1500-2000 ms: $t(200)=4.3$, $p=6.2e-05$), but not in Chat-Chrimson mice (Mixed-effects model, ANOVA: $F(4,130)=1.7$, $p=0.15$) or in control mice

(PV-tDTomato: Mixed-effects model, ANOVA: $F(4,170)=2.2$, $p=0.07$; Chat-tDTomato mice: Mixed-effects model, ANOVA: $F(4,150)=1.2$, $p=0.31$, n=4 tDTomato mice, and n=4 Chat-tDTomato mice, 2 sessions from each mouse). *=$p<0.05$, **=$p<0.01$, ***=$p<0.001$.

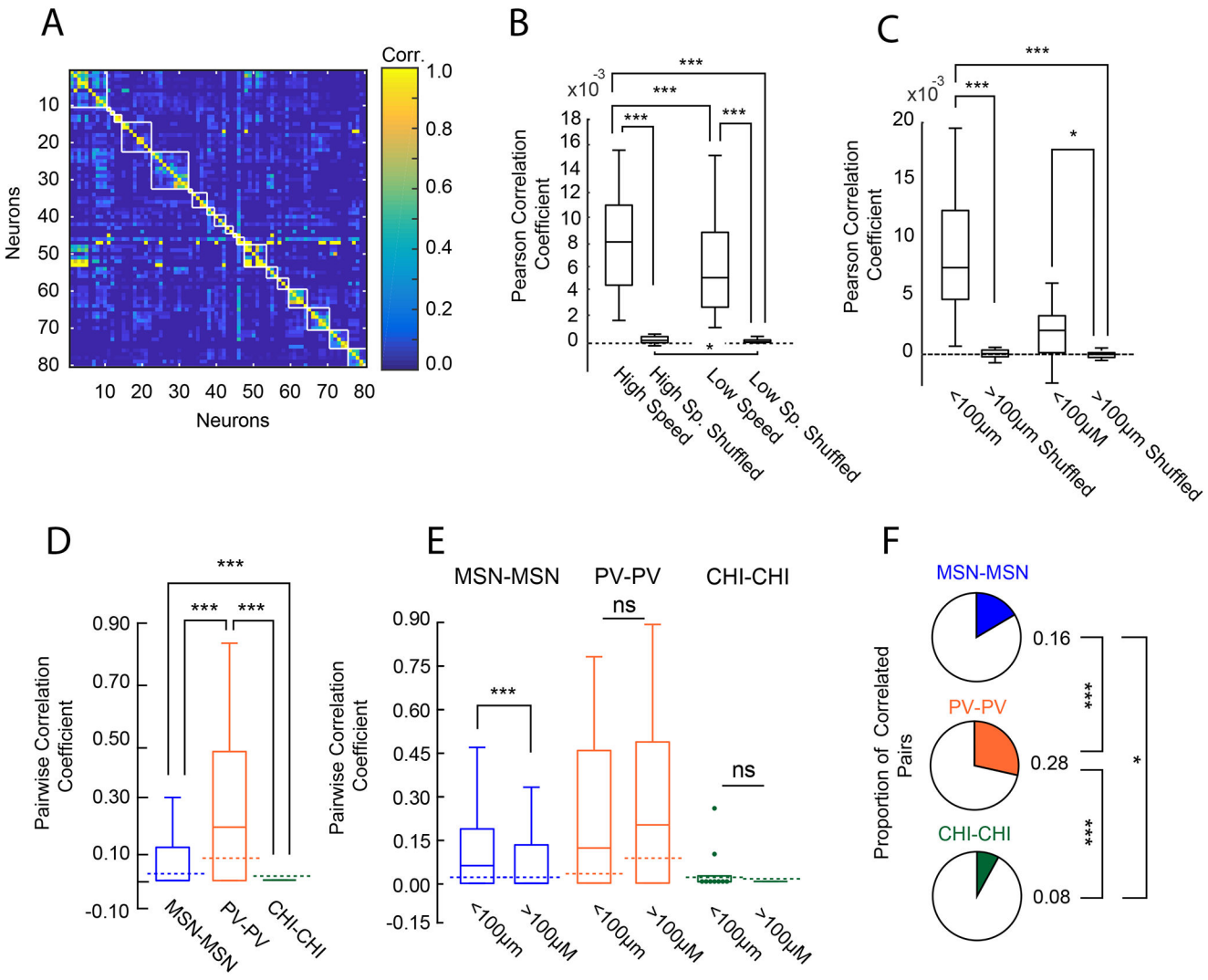

Figure 4: Anatomical Clustering and Coordinated Activity within each Cell Population.

(A) Correlation matrix utilizing asymmetric correlation coefficients of 80 neurons from a randomly chosen recording session. White lines represent boundaries between unique neuron pairs less than 100µm of one another. **(B)** Box plots of pairwise Pearson correlation coefficients during periods of high and low speed from all animals. Correlation between neuron pairs increased with speed (Sign-test, two-sided, sign=24, p=1.80e-04, n=28 sessions; high speed vs shuffled, sign=28, p=7.45e-09; low speed vs shuffled, sign=28, p=7.45e-09, high speed shuffled vs low speed shuffled: sign=21, n=28 sessions, p= 0.0125). **(C)** Difference in pairwise strength between periods of high and low movement sorted by anatomical distance across all cells from all sessions in all mice. The change in correlation strength was greatest between nearby cells (all two-sided sign-tests, sign-test, <100µm vs >100µm; sign=26, p=3.03e-06, n=28 sessions; sign-test, <100 µm vs <100 µm shuffled, sign=27, p=2.16e-07; sign-test, >100µm vs >100µm shuffled, sign=21, p=0.0125;). **(D)** Pairwise asymmetric correlation between the same cell types. Dotted lines indicate median of averaged correlation coefficients for within cell type shuffled data. PV cells showed the

highest correlation coefficient values (Kruskal-Wallis, $X^2(2)=1.5e+02$, p=7.69e-33; mean ranks: MSN: 7.46e+05, PV: 1.03e+06, CHI: 5.99e+05; Tukey's HSD post-hoc, MSN-MSN vs CHI-CHI: p=8.80e-06; MSN-MSN vs PV-PV: p=9.56e-10; PV-PV vs CHI-CHI: p=9.56e-10) and were correlated above that expected by chance based on within neuron type shuffled data (sign-test, sign=146, n=241 PV-PV pairs, p=0.0013) MSN-MSN pairs and CHI-CHI pairs were not significantly different from shuffled data. **(E)** Population box plots showing asymmetric pairwise correlation of each cell type across all 28 recording sessions sorted by anatomical distance. Dotted lines indicate median of averaged correlation coefficients for shuffled data for each cell pair. Pairs of MSNs in close proximity (<100 μm) are more correlated than those further apart. Unlike MSN pairs, PV pairs and CHI pairs were not modulated by distance (Effect of distance; two-sided Wilcoxon rank-sum, MSN-MSN pairs, w=5.3e10, $n_{<100}$=62895, $n_{>100}$=1429304, p=0; PV-PV pairs: w=1955, $n_{<100}$=17, $n_{>100}$=224, p=0.71; CHI-CHI pairs, w=684,$n_{<100}$=9, $n_{>100}$=143, p=1.0). As expected, only MSN pairs within 100μm were more correlated than chance based on within neuron-class shuffled data (sign-test, MSN-MSN pairs < 100 μm, sign=32864, n=62894 MSN-MSN pairs, ties = 1, p=1.37e-29; PV-PV pairs >100 μm, sign=137, n=224 PV-PV pairs, p=0.0011. All other comparisons were not different from chance based on shuffled data. **(F)** Population pie charts showing the number of significantly correlated pairs of neurons above those expected by chance from shuffled data, sorted by cell type. A greater proportion of PV cell pairs were correlated than MSN pairs, and both were more correlated than CHI pairs (MSNs vs. CHIs: $X^2(1)=7.2$, p=0.022; PVs vs. CHIs: $X^2(1)=26.3$, p=8.72e-07; MSN-MSN: 238293/1501649 pairs, PV-PV: 68/244 pairs, CHI-CHI: 13/160 pairs). For all box plot figures, middle lines indicate the median, lower and upper edges of the box indicate quartiles below and above the median, and upper and lower whiskers indicate the points furthest from the median whose value did not exceed 1.5 times the first-to-third quartile range above the third quartile or below the first quartile.

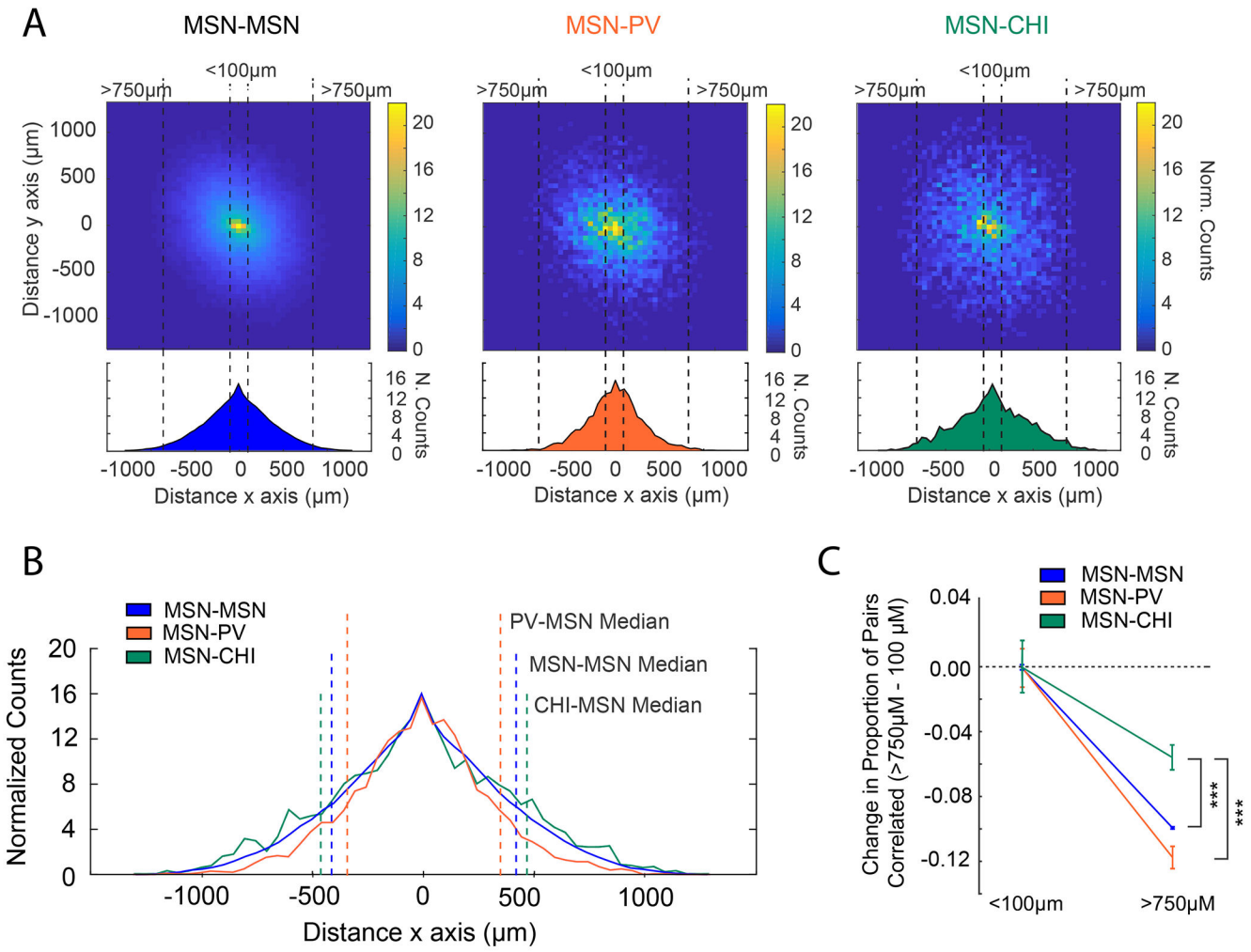

Figure 5: Coordinated Activity between Interneurons and MSNs by Anatomical Distance.

(A) Population colormaps from all sessions in all animals showing significantly correlated cell pairs sorted by distance. Density distributions from above in the x-axis are shown below. MSN-MSN cell pairs (left) and MSN-Interneuron cell pairs (PV, middle; CHI, right). MSN-CHI cells are correlated over greater distances than MSN-MSN pairs, and MSN-PV are correlated over smaller distances than MSN-MSN pairs (MSN-MSN median = 411µms, MSN-PV: 343 µms, MSN-CHI: 448 µms; Kruskal-Wallis, $X^2(2)=303$, $n_{MSN-MSN}=238293$, $n_{MSN-PV}=4028$, $n_{MSN-CHI}=2686$, p=1.87e-66; mean ranks: MSN-MSN: 1.23e+05, MSN-PV: 1.04e+05, MSN-CHI: 1.31e+05; Tukey's HSD post-hoc, MSN-PV vs MSN-MSN: p=9.56e-10, MSN-PV vs MSN-CHI: p=9.56e-10, MSN-MSN vs MSN-CHI: p=9.53e-09). **(B)** Population density distributions showing the x-direction from (A) for all cell types superimposed. The median value distance value from (A) has been plotted for reference on the x-direction plot. **(C)** Measure of the expected values between the proportion of significantly correlated pairs for the MSN-MSN, MSN-PV, and MSN-CHI populations for those separated by a distance of >750 µm vs < 100 µm. Data >750 µm are plotted relative to <100 µm values. For all interneuron-MSN combinations, the proportion of correlated pairs decreased as the distance between cells increased, though the decrease in CHI-MSN pairs

was more modest than that seen for PV-MSN or MSN-MSN pairs. Center indicates expected value, error bars are ± SE (Generalized linear model, Binomial family with identity link function; 274589 total observations; Benjamini-Hochberg corrected p-values of interaction terms (two-sided t-tests): MSN-MSN vs MSN-CHI: $t(274583) = 4.07$, $p=1.39e-04$; MSN-MSN vs MSN-PV: $t(274583) = -0.56$, $p=0.573$; MSN-PV vs MSN-CHI: $t(274583) = -3.42$, $p=9.53e-04$). All comparisons are made using pairwise data across 28 sessions in 12 Animals (6 PV-Cre animals and 6 Chat-Cre animals). *=$p<0.05$, ***=$p<0.001$.

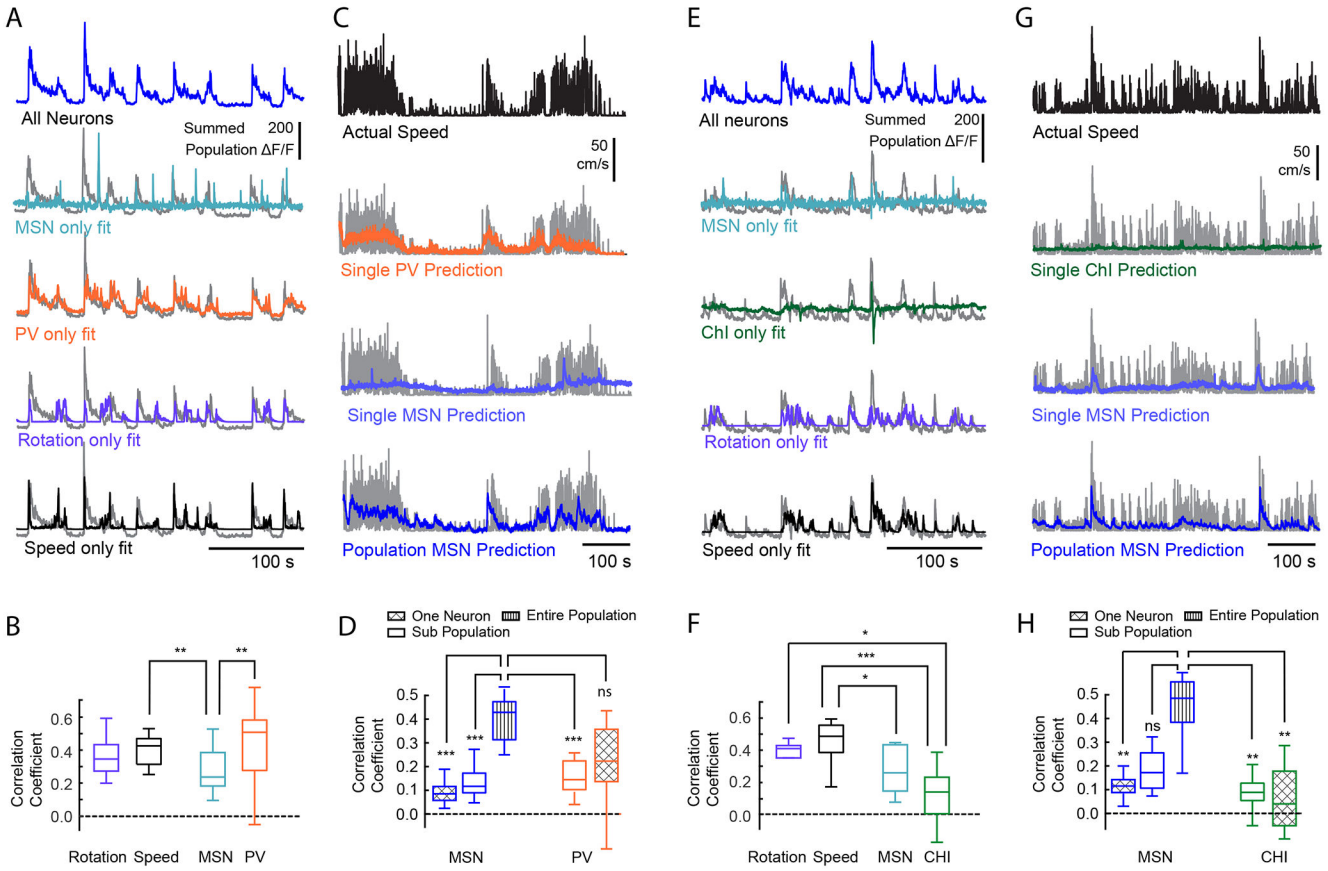

Figure 6: PVs, but not CHIs, are Strong Predictors of Speed and MSN Population Activity.

(A) Striatal population fluorescence (blue, top, and gray in the bottom four) and predicted fluorescence based on the PV activity (orange), or an equivalent number of MSNs (teal) from a representative PV-Cre mouse. **(B)** Quantification across all PV-Cre mice. Predictions of population fluorescence were compared to that derived from using motor output (rotation: purple; speed: black). PV Ca^{+2} dynamics were better predictors than that of an equivalent number of MSNs, and similar to speed and rotation Friedman test, $X^2(3)=18.0$, p=4.47e-04, n=17 sessions in 6 mice; mean ranks: speed: 2.94, rotation: 2.53, PV: 3.12, MSN: 1.41; post-hoc Tukey's HSD, speed vs PV: p=1.0, rotation vs PV: p=0.54; PV vs. MSNs, p=6.8e-04. **(C)** Actual speed and predicted speed based on PV cell activity or MSN activity for a representative PV mouse. Experimentally measured speed is plotted in black (top), and gray (bottom three), compared with predicted velocity using the activity of a single PV (orange), a single MSN (light blue) and the full population MSNs activity (dark blue). **(D)** Quantification of the population predictor performance across all PV-Cre mice. The ability of the full PV population from each recording session to predict speed was also compared to an equivalent number of MSNs (n=4.6±0.86 PV cells across 17 sessions with at least 1 PV cell, mean±SEM), referred to as "sub-population". The activity of a single PV was a significant predictor of speed, and the small population of PVs has equal predicting power speed as the entire population of MSNs (Friedman test, $X^2(4)=50.1$, p=3.51e-10; mean ranks: single MSN: 1.32, multiple MSN: 2.56, all MSN: 4.94, multiple PV: 3.56, single PV: 2.62, n=17 sessions; Tukey's HSD post-hoc: MSN all-MSN single: p=1.01e-08; MSN all-

MSN subgroup: p=9.12e-05, MSN all-PV all: p=0.076). **(E, F)** Same as (A, B) except for CHI neurons in Chat-Cre mice. Unlike PVs, CHI Ca^{+2} dynamics were poor predictors of population fluorescence. Friedman test, X^2 (3) = 24, p=2.50e-05, n =10 sessions in 6 mice; mean ranks: speed: 3.9, rotation: 2.7, CHI: 1.1, MSN: 2.3; Tukey's HSD post-hoc: speed vs. CHI: p=7.36e-06; rotation vs CHI: p=0.029; MSN vs CHI, p=0.16. **(G, H)** Same as (C, D) except from a representative Chat-Cre mouse **(G)** and predictor performance quantification for all Chat-Cre mice **(H)**. Actual speed is shown in black or gray. Predicted speed based on the activity of a single CHI neuron in green, a single MSN in light blue, or population MSNs in dark blue. Sub populations represent an equivalent number of MSNs as the full CHI population from each recording session (n = 5.1±1.1 CHIs across all recording sessions, mean±SEM). CHIs were weak predictors of speed, and using the full population of CHI cells did not significantly improve the predictive power over a single CHI. (Friedman test, $X^2(4)=20.8$, p=3.44e-04; mean ranks: single MSN: 2.5, multiple MSN: 3.4, all MSN: 4.8, multiple CHI: 2.2, single CHI: 2.1, n=10 sessions in 6 mice; Tukey's HSD post-hoc; MSN all-MSN single: p=0.0090, MSN all-CHI single: p=0.0011; MSN all-CHI all: p=0.0019, CHI all-CHI single: p=1.0). *=p<0.05, **=p<0.01, ***=p<0.001. For all box plot figures, middle lines indicate the median, lower and upper edges of the box indicate quartiles below and above the median, and upper and lower whiskers indicate the points furthest from the median whose value did not exceed 1.5 times the first-to-third quartile range above the third quartile or below the first quartile.

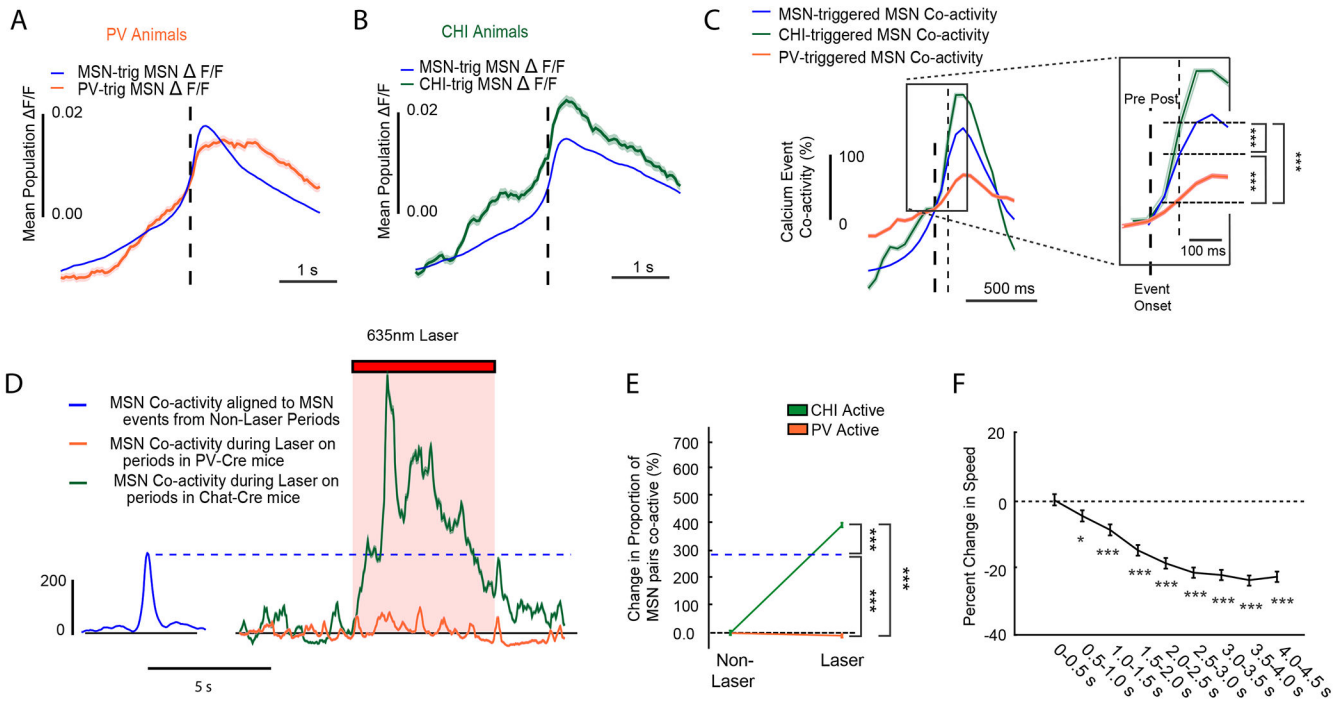

Figure 7: Interneurons Regulate MSN Activity and Movement State.

(A) MSN population fluorescence aligned to all PV calcium event onsets (orange) versus MSN calcium event onsets (blue) from all PV-Cre animals. MSN population peak fluorescence was significantly reduced in the 500ms following a PV calcium event (PV post-event: rank-sum test, two-sided, ranksum=2.43e+12 n_{PV}=237528 event-neurons, n_{MSN}=20289773 event-neurons, across all 6 PV animals and 18 sessions, p=1.48e-06), in comparison to a MSN calcium event (blue). Plots are mean ±SEM. **(B)** Same as (A) but for Chat-Cre animals. MSN peak population fluorescence was significantly elevated in the 500ms following a CHI calcium event (green: Chat-Cre post-event: two-sided, rank-sum test, ranksum=1.73e+12, p=2.53e-09, n_{MSN}=22116844 event-neurons, n_{CHI}=153680 event-neurons from 10 sessions in 6 animals), compared to an MSN event (blue). **(C)** Change in coincident MSN activity (MSN co-activity) following a MSN calcium event (blue), a PV calcium event (orange), or a CHI calcium event (green) from all animals and normalized to event onset for all three types (t=0). Plots are mean ±SEM. A magnified inset demonstrating the change in MSN co-activity probability in the 100ms following a MSN, PV or CHI calcium event is shown to the right. Following a CHI calcium event, there is an increase in MSN co-activity, whereas following a PV calcium event, there is a reduction in MSN co-activity relative to the change in MSN-triggered co-activity (Pairwise two-sided z-tests, PV-MSN vs CHI-MSN, z=−40.8, p=0; PV-MSN vs MSN-MSN, z=−47, p=0; CHI-MSN vs MSN-MSN, z=20.4, p=0. Bonferroni corrected post-hoc for multiple comparisons; raw proportions: MSN: 3.52e-03, PV:2.30e-03, CHI:5.91e-03,n_{CHI}=38189238, n_{CHI}=38189238 event-pairs, n_{MSN}=9644946557 event-pairs, n_{PV}=48285061 event-pairs, across all 12 animals and 28 sessions). **(D)** A time series showing MSN-MSN event co-activity during laser stimulation of PV cells (orange) and CHIs (green) during laser stimulation in PV-Chrimson mice (n=4 PV-Chrimson mice and n=4 Chat-Chrimson mice). For reference, the

change in MSN-MSN co-activity around random MSN events from all time periods outside of optogenetic stimulation for all PV-Chrimson and Chat-Chrimson mice is shown in blue. Plots are mean ±SEM. **(E)** Population line plots quantifying the change in the MSN-MSN co-activity upon optogenetic stimulation of PVs or CHIs in PV-Chrimson and Chat-Chrimson mice. Opto-stim induced co-activity was compared to the endogenous rate of MSN-MSN co-activity from the non-opto stimulation periods of the imaging session, indicated by the dashed blue line. Error bars and center are mean ± SEM. During optogenetic stimulation of CHIs MSN-MSN co-activity increased, whereas during optogenetic stimulation of PVs, MSN-MSN co-activity decreased, relative to the endogenous MSN-MSN co-activity rate (Pairwise two-sided z-tests, n_{CHI}=2078751 event-pairs, n_{MSN}=694475807 event-pairs, n_{PV}=682922 event-pairs; CHI-MSN vs PV-MSN z=78.7, p=0; MSN-MSN vs MSN-PV, z=−228, p=0; MSN-MSN vs CHI-MSN, z=19.2,p=0, n=4 PV-Chrimson mice and n=4 Chat-Chrimson mice, Bonferroni corrected post-hoc for multiple comparisons). *=p<0.05, **=p<0.01, ***=p<0.001. **(F)** Change in movement speed after peaks in MSN-MSN co-activity events (see supplemental methods), binned into 500ms windows for analysis. Error bars and center are mean ± SEM. Peaks in MSN co-activity were followed by decreases in speed similar to that observed following CHI events, and CHI optogenetic stimulation (Friedman test, main effect of time, n=2249 peaks in coactivity, $X^2(8)$=520, p<0.001; Tukey's HSD post-hoc, (vs 0-0.5 s) 0.5-1 seconds, p=0.030, 1.00-1.50 seconds, p=9.30e-07, 1.50-4.50 seconds, all p=8.97e-08; mean ranks: 5.81, 5.54, 5.35, 5.04, 4.84, 4.72, 4.62, 4.52, and 4.56).